JPhys Energy

PAPER • **OPEN ACCESS**

Design of n-i-p and p-i-n Sb_2Se_3 solar cells: role of band alignment

To cite this article: Marwa S Salem *et al* 2023 *J. Phys. Energy* **5** 045007

IOP Publishing J. Phys. Energy 5 (2023) 045007 https://doi.org/10.1088/2515-7655/acf688

Journal of Physics: Energy

CrossMark

OPEN ACCESS

RECEIVED
2 May 2023

REVISED
7 August 2023

ACCEPTED FOR PUBLICATION
4 September 2023

PUBLISHED
14 September 2023

PAPER

Design of n-i-p and p-i-n Sb_2Se_3 solar cells: role of band alignment

Marwa S Salem[1,2], **Mohamed Okil**[3], **Ahmed Shaker**[4,*], **Abdullah Albaker**[5] and **Mansoor Alturki**[5]

[1] Department of Computer Engineering, College of Computer Science and Engineering, University of Ha'il, Ha'il 55211, Saudi Arabia
[2] Department of Electrical Communication and Electronics Systems Engineering, Faculty of Engineering, Modern Science and Arts University (MSA), Cairo 12556, Egypt
[3] Department of Basic Engineering Sciences, Benha Faculty of Engineering, Benha University, Benha 13512, Egypt
[4] Department of Engineering Physics and Mathematics, Faculty of Engineering, Ain Shams University, Cairo 11535, Egypt
[5] Department of Electrical Engineering, College of Engineering, University of Ha'il, Ha'il 81451, Saudi Arabia
[*] Author to whom any correspondence should be addressed.

E-mail: ahmed.shaker@eng.asu.edu.eg

Keywords: Sb_2Se_3, ETL, HTL, band alignment, CBO, VBO, PCE

Supplementary material for this article is available online

Abstract

Investigations into novel device architectures and interfaces that enhance charge transport and collection are necessary to increase the power conversion efficiency (PCE) of antimony selenide (Sb_2Se_3) solar cells, which have shown great promise as a low-cost and high-efficiency alternative to conventional silicon-based solar cells. The current work uses device simulations to design p-i-n and n-i-p Sb_2Se_3-based solar cell structures. The n-i-p configuration is investigated by comparing distinct electron transport layer (ETL) materials to get the best performance. While certain ETL materials may yield higher efficiencies, the J–V curve may exhibit S-shaped behavior if there is a misalignment of the bands at the ETL/absorber interface. To address this issue, a proposed double ETL structure is introduced to achieve proper band alignment and conduction band offset for electron transport. A PCE of 20.15% was achieved utilizing (ZnO/ZnSe) as a double ETL and Spiro-OMeTAD as a hole transport layer (HTL). Further, the p-i-n configuration is designed by proposing a double HTL structure to facilitate hole transport and achieve a proper valence band offset. A double HTL consisting of (CuI/CuSCN) is used in conjunction with ETL-free configuration to achieve a PCE of 21.72%. The simulation study is conducted using the SCAPS-1D device simulator and is validated versus a previously fabricated cell based on the configuration FTO/CdS/Sb_2Se_3/Spiro-OMeTAD/Au.

1. Introduction

Solar cells are a key renewable energy resource that has gained significant attention in recent years due to their potential to address the challenges of climate change, energy security, and sustainability. The energy generated by solar cells is free, abundant, and widely available, making them an ideal solution for meeting the growing electricity demand. In recent years, photovoltaic (PV) technology has advanced rapidly, resulting in increased efficiency, reduced costs, and improved reliability [1, 2]. Silicon solar cells are the most commonly employed and mature PV technology, accounting for more than 90% of the global market [3]. Silicon solar cells have several advantages, including high efficiency, long lifespan, and low maintenance requirements. They are also environmentally friendly [4]. In recent years, research has focused on improving silicon solar cells' efficiency through advanced manufacturing techniques, such as passivation and surface texturing, as well as the incorporation of new structures [3–5]. Alternatively, thin film solar cells (TFSCs) are a type of PV technology that uses thin layers of semiconductor materials [6]. Unlike traditional silicon solar cells, TFSCs are flexible, lightweight, and can be produced at lower costs, making them an attractive option for many applications. TFSCs use less material than traditional silicon solar cells, making them cheaper to produce. They can also be produced using roll-to-roll manufacturing techniques, allowing for high-volume and low-cost production [7]. However, TFSCs typically have lower efficiencies than silicon solar cells, which can limit their effectiveness in some applications.

Some thin film materials also contain toxic elements, such as cadmium or lead, which can pose environmental risks if not handled properly [8]. One of the most promising candidates for use in TFSCs is antimony selenide (Sb_2Se_3), a semiconductor material that has recently gained interest in the field of solar cells [9]. PV devices based on Sb_2Se_3 have shown promising results because of their unique properties, such as high absorption coefficient, suitable bandgap, and favorable carrier transport characteristics [10]. According to [11], the bandgap of Sb_2Se_3 falls within the range of 1.1–1.3 eV, while the carrier mobility has been reported to be in the range of 50–300 $\text{cm}^2\ (\text{V s})^{-1}$ [12]. In addition, the carrier lifetime has been reported to be on the order of nanoseconds to microseconds, while the optical absorption coefficient is around 10^4–10^5 cm^{-1} [12]. Moreover, Sb_2Se_3 is an abundant and low-cost material, which makes it an attractive option for the large-scale production of solar cells [12]. In this context, the use of Sb_2Se_3 as an absorber material in solar cells has been extensively investigated by researchers worldwide, where over a few years, the power conversion efficiency (PCE) of Sb_2Se_3-based solar cells has significantly increased from less than 3% to approximately 10.57% [13–16], demonstrating the significant potential of Sb_2Se_3 as a material for PV applications.

Several research works have aimed to develop Sb_2Se_3-based PV cells, utilizing different methods such as close-spaced sublimation, atomic layer deposition, and hydrothermal deposition. These studies have employed various electron and hole transport layers, resulting in a range of efficiencies from 6.5% to 9.2% [17–19]. The transport layers are avoided in order to prevent the interface issues related to the mismatch between the absorber and these layers. In this regard, PCEs of 6.7 and 7.6% were achieved with hole transport layer (HTL)-free substrate and n-i-p structures, respectively [20, 21]. Recently, Chen *et al* provided an effective doping strategy for optimizing the physical properties of the Sb_2Se_3 absorber and, therefore, the further efficiency advancement of the Sb_2Se_3-based solar devices [22]. The PCEs reported in the literature of Sb_2Se_3 PV cells still lag behind the theoretical PCE limit, which is almost 27% [23]. Many key cell parameters must be explored to enhance cell performance, as the recorded PCE of Sb_2Se_3 PV cells is still below the theoretical limit, indicating the need for further optimization.

To conserve time and experimental work, numerical simulations are necessary to identify the key design parameters and suggest practical solutions. However, few studies have investigated p-i-n and n-i-p structures for Sb_2Se_3 cells. Numerous efforts were conducted to simulate Sb_2Se_3-based solar cells with different electron and hole transport layer materials [23–28]. However, few studies have investigated p-i-n and n-i-p structures for Sb_2Se_3 solar cells. For example, Cao *et al* proposed and simulated a p-i-n Sb_2Se_3 cell in an inverted ITO/NiO/Sb_2Se_3/PCBM/Ag architecture and reported a PCE of 19.6% with suppressing the defect states and an absorber thickness of 0.5 μm [25]. Further research is needed to determine the optimal structure for Sb_2Se_3 cells.

In this paper, p-i-n and n-i-p Sb_2Se_3-based solar cells will be designed using a SCAPS device simulator [29]. The work utilizes calibration and extraction of material parameters based on experimental studies. Different key parameters are optimized based on technological constraints related to fabrication. The initial validation of the simulation model is performed by comparing the simulation results with a formerly fabricated cell based on the configuration FTO/CdS/Sb_2Se_3/Spiro-OMeTAD/Au [16]. Although the short-circuit current (J_{sc}) of this cell is relatively high, its open-circuit voltage (V_{oc}) is relatively low, indicating a need for improvement in the cell design. Thus, we investigate two different Sb_2Se_3 cell configurations to improve the V_{oc}, and thus enhance the cell performance. The n-i-p configuration is investigated to achieve a proper band alignment between the absorber and the contact through the design of the electron transport layer (ETL). In addition, the cell performance is compared with and without HTL. Moreover, the p-i-n structure is explored to optimize the band alignment by the design of the HTL to attain a proper valence band offset (VBO). Also, the cell performance is compared with and without ETL. All simulations are performed in the SCAPS-1D software platform under the illumination of 1-sun AM1.5G.

2. Simulation methodology and device structure

2.1. Simulation approach

In this study, the SCAPS-1D simulator, researched at the electronics and information systems department of Gent University, is exploited to design, and evaluate the Sb_2Se_3-based solar cell. The simulator has been employed extensively to model and simulate thin-film solar cells [30–35]. Figure 1 depicts a flowchart of the SCAPS simulator, illustrating the main semiconductor equations and the necessary input physical and geometrical parameters. The simulator concurrently solves Poisson's equation and electron and hole continuity equations. The drift-diffusion transport model is then utilized to evaluate the current densities of the carriers. Regarding recombination statistics, the simulator provides the option to choose the

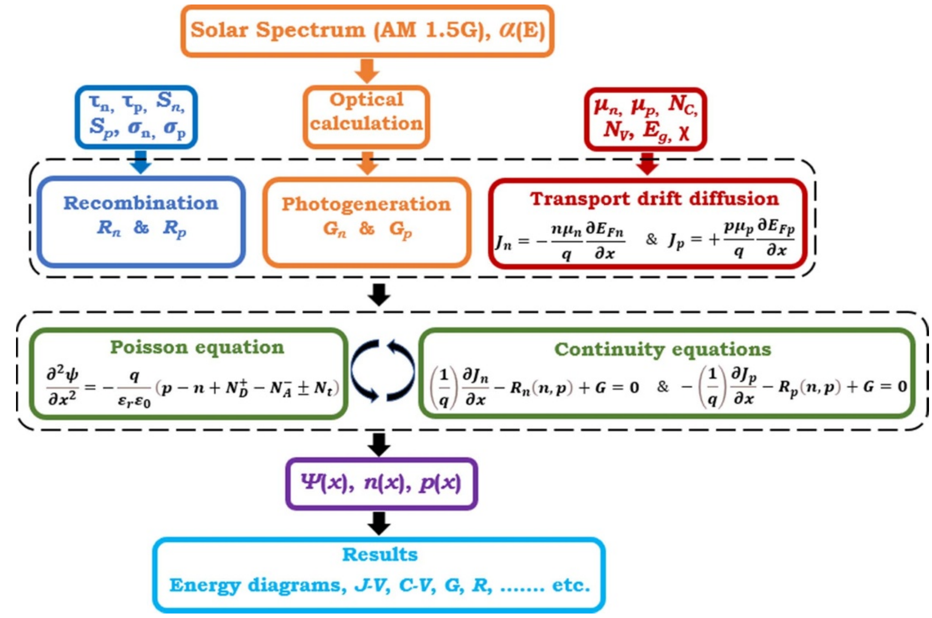

Figure 1. SCAPS-1D simulator flowchart indicating the involved input parameters along with the main semiconductor equations.

Shockley-Read-Hall (SRH) and/or Auger mechanisms. However, in our simulation, we solely employ the SRH mechanism. SCPAS-1D software is well suited for thin film PV cells as it has demonstrated satisfactory results and has been extensively validated against various types of experimental thin film cells [31–34, 36, 37]. The definitions of primary input and output technological parameters from SCAPS-1D are recorded in table S1 in the supplementary materials and their definitions.

2.2. Device configuration and material parameters

The cell construction of the Sb_2Se_3-based solar cell and energy band profiles before and after contact are exhibited in figure 2. The solar cell is composed of thin layers, as follows. A work function of 4.7 eV is set for the FTO front contact. The back contact is Au with a work function of 5.1 eV. The ETL material is CdS, while Spiro-OMeTAD acts as an HTL. Table 1 summarizes the major parameters of the cell layers used in this study, which are extracted from published studies. In addition, the boundary conditions of the two contacts were considered to satisfy thermionic emission, and the electron and hole surface recombination velocities are specified in table S2 of the supplementary material. The thermal velocities of electrons and holes are set to 1×10^7 cm s^{-1} for all layers.

Furthermore, single, and neutral defects with a trap defect density of 5×10^{12} cm^{-2} are considered for the CdS/Sb_2Se_3 and Sb_2Se_3/Spiro-OMeTAD interfaces. The other defect factors at these interfaces are summarized in table S3 in the supplementary material. The bulk defects within the Sb_2Se_3 absorber are recorded in table 2 based on experimental reports [16]. While conducting our simulations using the SCAPS simulator, it is important to acknowledge that the tool does not account for advanced effects related to anisotropy, which is a unique characteristic in quasi-2D materials like Sb_2Se_3. The illuminated current density–voltage (J–V) characteristics of simulated and experimental Sb_2Se_3 cells [16] are presented in figure 3(a), utilizing the listed parameters. The simulated PV parameters match the experimental data as revealed in table 3, indicating the validation of the simulation from SCAPS-1D. In addition, the external quantum efficiency (EQE) curves of simulated and experimental Sb_2Se_3 cells [16] are presented in figure S1. The absorption spectra of transport layers (CdS and Spiro-OMeTAD) are incorporated from SCAPS, where the corresponding files for these materials are readily available in the SCAPS database. For Sb_2Se_3, we used the square root model implemented in SCAPS and the absorption coefficient is computed using equation (1),

$$\alpha(\lambda) = \left(A + \frac{B}{f}\right)\sqrt{hf + E_g}. \tag{1}$$

Here, E_g is the material bandgap, and A (in cm^{-1} $eV^{-1/2}$) and B (in cm^{-1} $eV^{+1/2}$) are model parameters. This approach is verified when comparing the measured J_{sc} with the corresponding simulation value. The values of A, B and band tail are 2.967×10^5 cm^{-1} $eV^{-1/2}$, 1.095×10^{-12} cm^{-1} $eV^{+1/2}$ and 20 meV,

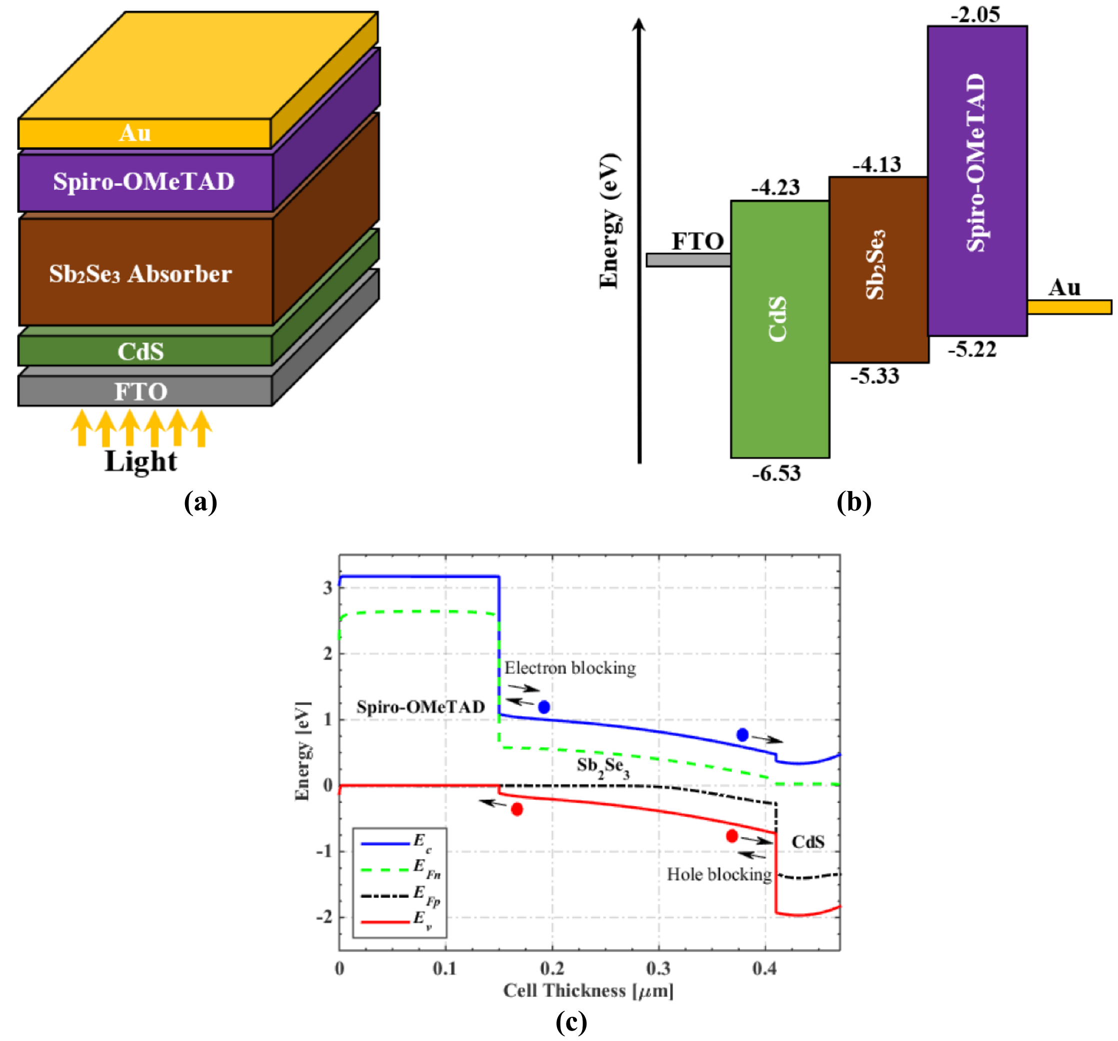

Figure 2. Typical FTO/ETL/Sb_2Se_3/HTL/Au cell configuration: (a) main layers (CdS serves as an ETL and Spiro-OMeTAD acts as an HTL), (b) energy band profile before contact illustrating the accompanying energy levels of each thin film, and (c) energy band diagram after contact at short circuit current condition under AM1.5G illumination.

Table 1. Key technological parameters of the various layers of the Sb_2Se_3-based PV cell.

Parameters	CdS	Sb_2Se_3	Spiro-OMeTAD
t (nm)	60	260	150
E_g (eV)	2.3	1.2	3.17
χ (eV)	4.23	4.13	2.05
ε_r	10	10	3
μ_n ($cm^2 V s^{-1}$)	100	5	2×10^{-4}
μ_p ($cm^2 V s^{-1}$)	25	1.5	2×10^{-4}
N_c (cm^{-3})	2.2×10^{18}	2.2×10^{18}	2.2×10^{18}
N_v (cm^{-3})	1.9×10^{19}	1.8×10^{19}	1.8×10^{19}
N_D (cm^{-3})	1×10^{17}	—	—
N_A (cm^{-3})	—	7.25×10^{15}	2×10^{19}
References	[32]	[16, 32]	[34]

respectively. Also, upon slightly changing these values, a good match between our simulation and the experimental *EQE* is obtained, as clarified in figure S1. It is noted that the integrated current density from *EQE* curves was 30.71 mA cm^{-2}, which was lower than the J_{sc} obtained from the corresponding *J*–*V* curves (33.52 mA cm^{-2}). This mismatching of J_{sc} between the *EQE* curves and the *J*–*V* curves can also be observed in previous studies of Sb_2Se_3 solar cells [19, 38].

Table 2. Defects parameters of the Sb_2Se_3 applied in device simulation [16].

Parameter	Defect 1	Defect 2
Defect type	Single acceptor ($0/^-$)	Single acceptor ($0/^-$)
Energetic distribution	Gaussian	Gaussian
Capture cross section (cm^2)	3.23×10^{-17}	3.3×10^{-15}
Energy level (eV)	0.609 (above E_v)	0.691 (above E_v)
Total density (N_t) (cm^{-3})	1×10^{13}	4.27×10^{12}
Electron diffusion length (L_n) (μm)	63	9.6
Hole diffusion length (L_p) (μm)	35	5.3

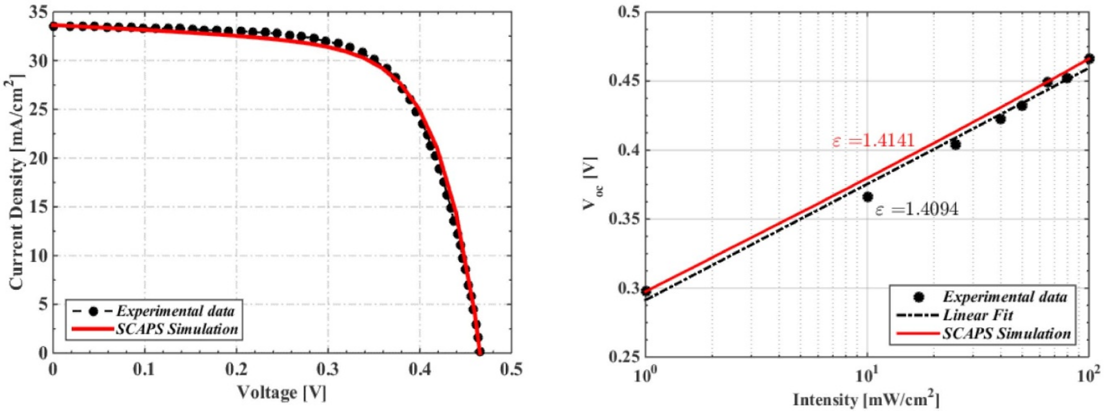

(a) (b)

Figure 3. Calibration of simulation versus experimental data [16] (a) *J–V* curves under AM1.5G illumination, and (b) the dependencies of V_{oc} and J_{sc} on *I*.

Table 3. PV parameters extracted from illuminated *J–V* curves for experimental and simulated data [16].

PV Parameters	V_{oc} (V)	J_{sc} (mA cm^{-2})	*FF* (%)	*PCE* (%)
Experimental data	0.467	33.52	67.64	10.57
SCAPS simulation	0.466	33.64	67.06	10.51

In order to further confirm the model accuracy, the relationship between V_{oc} and light intensity (I) based on simulation against measurements [16] is exhibited in figure 3(b). Remarkably, V_{oc} can be theoretically formulated as a function of I using equation (2) [39],

$$V_{oc} = \varepsilon V_T \ln(I) + \text{constant} \tag{2}$$

where V_T and ε are the thermal voltage and the ideality factor, respectively. As all photo-excited carriers recombine in the absorber film at open circuit conditions, determination of the carrier recombination mechanism is possible based on equation (2). It was found that a solar cell shows extra SRH recombination rates if ε is greater than 1 [39, 40]. As is depicted in figure 3(b), the values of ε were computed as 1.4094 and 1.4141 for experimental and simulated solar cells, respectively.

3. Results and discussion

3.1. Sb_2Se_3 cell with n-i-p configuration

In this subsection, we investigate the performance of the n-i-p Sb_2Se_3 solar cells. The proposed cells have the following configurations: single and double ETL. For the single ETL structures, various ETL materials are explored with and without HTL. In addition, regarding the double ETL structures, in which two electron transport layers are designed, some selected materials are simulated within the solar cell to provide the best band alignment throughout the cell. The simulation is also done with and without HTL. In all investigated devices, the top and bottom contacts are FTO and Au, respectively.

3.1.1. Single ETL versus double ETL

To achieve high-performance n-i-p Sb_2Se_3-based solar cells, the materials used in the ETL design must possess specific properties. These properties include a high value for the work function to match the energy

Table 4. Fundamental physical parameters of various inorganic ETL materials.

Parameters	$Zn_{0.8125}Mg_{0.1875}O$	ZnO	IGZO	WS_2	ZnSe
t (nm)	60	60	60	60	60
E_g (eV)	3.65	3.2	3.05	1.8	2.81
χ (eV)	4.21	4.26	4.16	3.95	4.09
ε_r	9	9	10	13.6	8.60
μ_n ($cm^2\ V\ s^{-1}$)	50	200	15	100	400
μ_p ($cm^2\ V\ s^{-1}$)	20	5	0.1	100	110
N_c (cm^{-3})	1×10^{16}	2×10^{18}	5×10^{18}	1×10^{18}	2.2×10^{18}
N_v (cm^{-3})	1×10^{17}	1.8×10^{19}	5×10^{18}	2.4×10^{19}	1.8×10^{18}
References	[43]	[44]	[34]	[45]	[46]

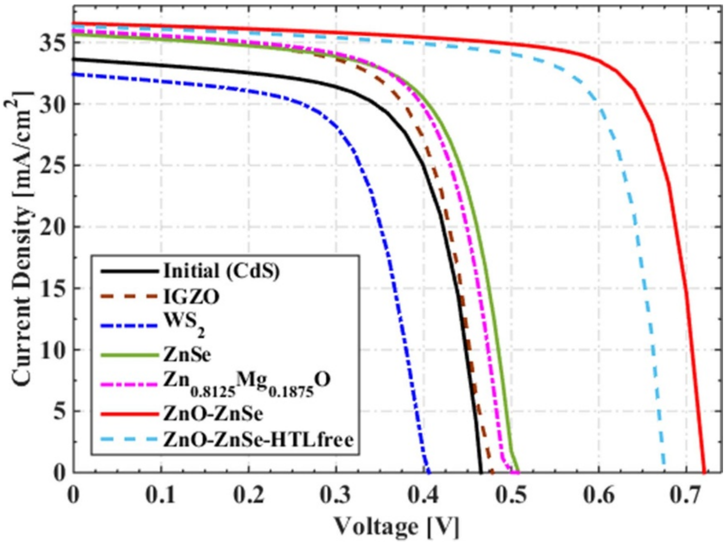

Figure 4. Illuminated *J*–*V* curves of n-i-p Sb_2Se_3 cell with various single and double ETL structures.

level of the Sb_2Se_3 layer and FTO, transparency to allow for better light absorption in the photoactive film, high electron mobility to ease electron transportation and reduce charge accumulation and recombination, and a wide bandgap to block hole carriers. While conventional CdS meets most of these criteria, its low bandgap and negative conduction band offset (CBO) result in lower V_{oc}, as previously noted. The heterojunction interface also plays a critical role in controlling recombination, electric field, and current flow on both sides of the heterojunction. Therefore, extra research is necessary to identify suitable ETL materials. CBO is essential in determining V_{oc} and cell efficiency, as defined in [41, 42] (see equation (3)), making it a crucial factor to consider in ETL analysis,

$$\mathrm{CBO} = \Delta E_c = \chi_{\text{absorber}} - \chi_{\text{ETL}}. \tag{3}$$

According to a previous study [41], the optimal CBO for a perovskite solar cell ranged from 0 to 0.3 eV. However, we do not believe that this choice provides a universal solution for other TFSCs. The numerical study was conducted with a high interface trap concentration, which may result in other effects being overshadowed by interface recombination. Table 4 displays the fundamental parameters of various ETL materials, selected to cover a range of CBO values. Figure 4 depicts the various ETL materials and their associated *J*–*V* characteristic curves under AM1.5G illumination.

The results show that ZnSe is the most suitable ETL material, owing to its favorable band alignments and high conductivity. Yet, the barrier height of the majority carriers between the ETL and front FTO contact is also critical and should not be overlooked. Table 5 presents the values of the majority barrier height (φ_n) for the various ETL materials. It should be noted that the S-shape behavior happens because of the band misalignment between the ETL and FTO contact, which can be explained by the value of φ_n. This misalignment creates an electric field that blocks electron transportation to the contact, resulting in more kink behavior. ZnSe has a lower S-shape trend, despite having the largest φ_n compared to other ETL materials, because it has the highest electron mobility. The barrier height and electron mobility dictate electron transport from the ETL to the front contact, with ZnSe showing the lowest kink effect overall.

Table 5. Band and PV parameters for n-i-p Sb_2Se_3 cell with various single and double ETL materials.

Cell configuration	ETL	φ_n	CBO	V_{oc} (V)	J_{sc} (mA cm^{-2})	*FF* (%)	*PCE* (%)
CdS/Sb_2Se_3/Spiro	Single	0.47	−0.1	0.466	33.64	67.06	10.51
CdS/Sb_2Se_3/HTL-free		0.47	−0.1	0.467	33.15	65.97	10.23
WS_2/Sb_2Se_3/Spiro		0.75	0.18	0.405	32.40	64.24	8.42
$Zn_{0.8125}Mg_{0.1875}O/Sb_2Se_3$/Spiro		0.49	−0.08	0.500	35.95	66.29	11.93
$IGZO/Sb_2Se_3$/Spiro		0.54	−0.03	0.478	35.78	66.18	11.32
$ZnSe/Sb_2Se_3$/Spiro		0.61	0.04	0.506	35.65	67.18	12.13
$ZnSe/Sb_2Se_3$/HTL-free		0.61	0.04	0.511	35.22	65.29	11.76
(ZnO-ZnSe)/Sb_2Se_3/Spiro	Double	0.44	0.04	0.720	36.46	76.72	20.15
(ZnO-ZnSe)/Sb_2Se_3/HTL-free		0.44	0.04	0.675	36.22	74.91	18.34

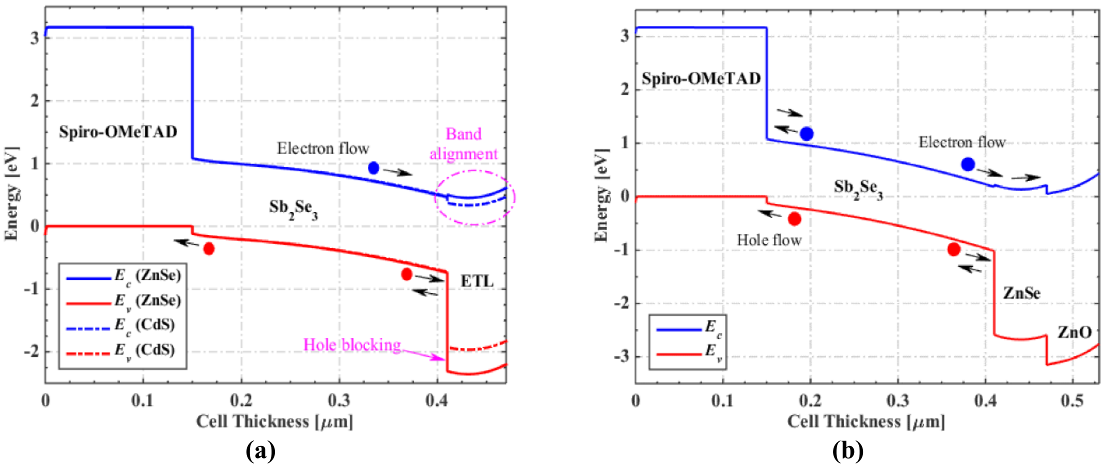

Figure 5. Energy band profile at short circuit current condition under AM1.5G illumination for n-i-p Sb_2Se_3 cell with different ETL architectures (a) single ETL (CdS & ZnSe), and (b) double ETL (ZnO/ZnSe).

For a comprehensive design of the investigated cell, it is desirable to eliminate the S-shape curve possibility resulting from the misalignment of the ETL material with the work function of the front FTO contact. Additionally, CBO engineering have to be pursued to accomplish the highest feasible PCE. This part explores the utilization of a dual ETL system, consisting of ZnSe as an adjacent layer to the Sb_2Se_3 absorber and ZnO as an additional ETL. Defect parameters at the ZnO/ZnSe interface are the same as for the ETL/absorber interface. Furthermore, the performance of the double ETL cell is analyzed both with and without an HTL, and the *J*–*V* curves of their output under illumination are depicted in figure 4. The outcomes indicate that the anticipated reduction of the S-shaped curve phenomenon has been achieved. Both variations of the double ETL design exhibit significant enhancements over the single ETL structure, which utilizes ZnSe as the ETL. The configuration that incorporates ZnO as the additional ETL displays greater improvement owing to its advantageous band alignments and elevated conductivity, in contrast to the structure that utilizes ZnSe as the sole ETL. The PV parameters of all the analyzed ETLs have been established and are presented in table 5.

3.1.2. Physical interpretation of the results

In order to provide a physical explanation for the observed trends when using either a single ETL or a double ETL, the energy band profiles have been created for three distinct cases: single ETL using CdS and ZnSe, and double ETL using ZnO/ZnSe, as illustrated in figure 5. Based on figure 5(a), it can be deduced that though ZnSe presents stronger hole blocking than CdS, its misalignment with the FTO contact creates a barrier that hinders electron transport due to its high φ_n. However, it exhibits a favorable band alignment with the absorber, resulting in an almost flat band. Conversely, figure 5(b) demonstrates that the combination of two ETLs aids in facilitating electron transport towards the FTO contact, as well as providing hole-blocking capabilities.

Furthermore, in order to offer a physical description for the decrease in performance parameters observed when utilizing a double ETL configuration with HTL-free, the recombination rate profile across the device distance at the illuminated short-circuit condition has been generated, as depicted in figure 6(a). The figure demonstrates that choosing a double ETL configuration is advantageous in terms of minimizing

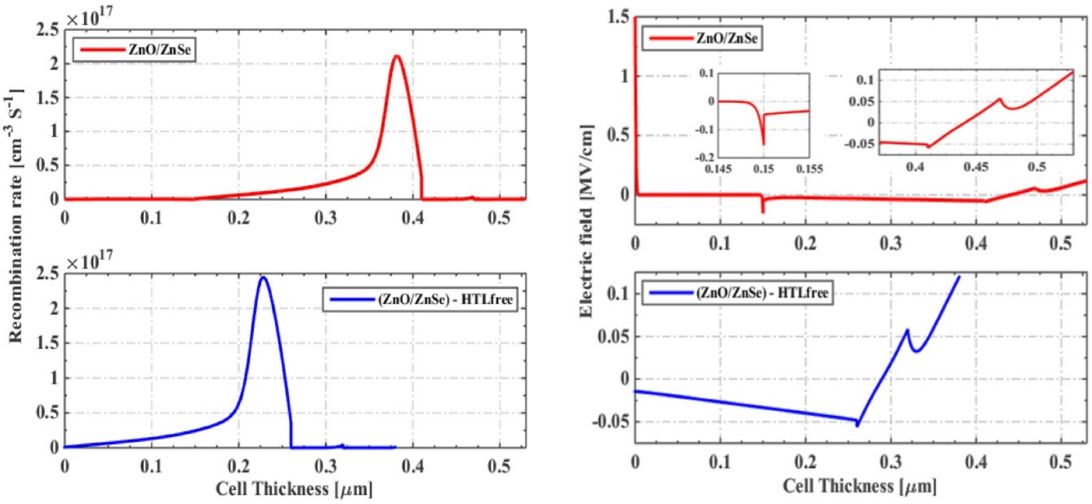

(a)

(b)

Figure 6. (a) Recombination rate profiles, and (b) electric field distribution plotted under illuminated short-circuit condition for n-i-p structure with double ETL with and without HTL.

recombination losses. However, when utilizing a double ETL configuration with HTL-free, the recombination rate in the absorber layer increases. The distribution of the electric field along the device structure, from HTL to ETL direction, at the illuminated short-circuit situation provides further support for the concept of recombination behavior. This distribution is displayed in figure 6(b). The figure reveals that the interface between the back contact and the HTL experiences the highest electric field in the case of a double ETL configuration. This is attributed to the HTL's heavily doped concentration which hinders the capture of free negative charge carriers at the back contact, leading to an increase in total current density. Moreover, there exists a negative peak at the interface between the HTL and absorber which aids the extraction of photogenerated holes from the absorber layer to the back contact. Consequently, the use of a double ETL configuration enhances the solar cell performance.

3.2. Sb_2Se_3 cell with p-i-n configuration

In this subsection, the performance of the p-i-n Sb_2Se_3 solar cells is studied. The proposed cells have the following structures: single and double HTL. For the single HTL cells, various HTL materials are assessed with and without HTL. Additionally, concerning the double HTL configurations, in which two hole transport layers are designed, some chosen materials are simulated to arrange for the best band alignment throughout the investigated cells. The simulation is also done with and without ETL. In all presented cells, the top and bottom contacts are FTO and Ag, respectively.

3.2.1. *Single HTL versus double HTL*

In order to produce high-performance p-i-n Sb_2Se_3-based cells, the materials utilized in the HTL design must possess specific characteristics. These characteristics include a high value of the work function to match the energy level of the Sb_2Se_3 layer and FTO, transparency to enable better light absorption in the absorber, higher hole mobility to make hole flow easier and reduce charge carrier recombination, and a large bandgap to prevent undesirable electron flow. Although conventional Spiro-OMeTAD fulfills most of these requirements, its low hole mobility and negative VBO result in lower V_{oc}, as previously stated. The VBO is vital in determining V_{oc} and cell efficiency, as described in [41] (equation (4)), rendering it a critical factor to consider in HTL analysis,

$$VBO = \Delta E_v = (E_g + \chi)_{HTL} - (E_g + \chi)_{\text{absorber}}. \tag{4}$$

A prior investigation [41], indicated that the optimal VBO for a perovskite solar cell was between 0 to 0.2 eV. Nonetheless, we do not believe that this selection offers a universal solution for other TFSCs as we explained here before. Table 6 showcases the essential parameters of various HTL materials that were chosen to encompass a range of VBO values. Figure 7 illustrates the distinct HTL materials and their respective *J*–*V* characteristics under illumination.

The findings indicate that the conventional HTL material (Spiro-OMeTAD) displays S-shape behavior because of the band misalignment between the HTL and FTO contact, attributed to the majority barrier

Table 6. Fundamental parameters of different inorganic HTL materials.

Parameters	CuSCN	NiO	CuI	CuO
t (nm)	75	75	75	75
E_g (eV)	3.6	3.8	3.1	2.1
χ (eV)	1.7	1.46	2.1	3.2
ε_r	10	10.7	6.5	7.11
μ_n (cm^2 V s^{-1})	100	12	100	3.4
μ_p (cm^2 V s^{-1})	25	2.8	43.9	3.4
N_c (cm^{-3})	2.2×10^{19}	2.8×10^{19}	2.8×10^{19}	2.2×10^{18}
N_v (cm^{-3})	1.8×10^{18}	1×10^{19}	1×10^{19}	1.8×10^{18}
References	[45]	[45]	[45]	[47]

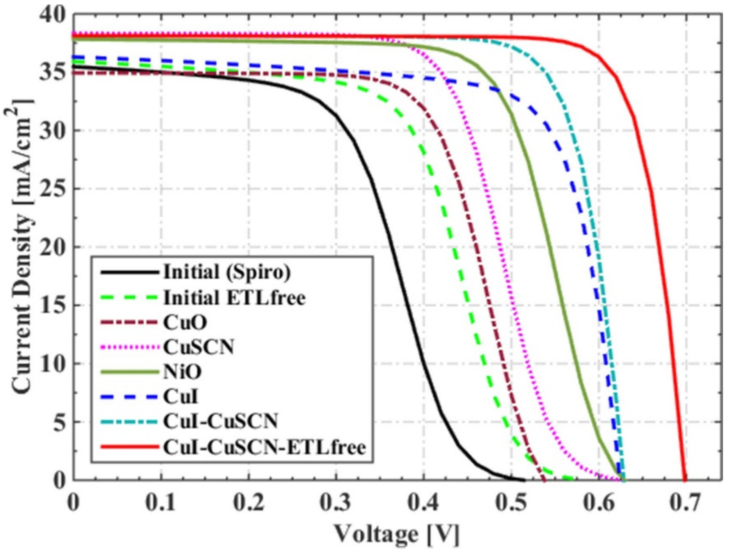

Figure 7. Illuminated *J–V* characteristics of p-i-n Sb_2Se_3 cell with different HTL layers.

Table 7. Band and PV parameters for p-i-n Sb_2Se_3 cell with various single and double HTL materials.

Cell configuration	HTL	φ_p	VBO	V_{oc} (V)	J_{sc} (mA cm^{-2})	*FF* (%)	*PCE* (%)
Spiro/Sb_2Se_3/CdS	Single	0.52	−0.11	0.511	35.46	51.47	9.33
Spiro/Sb_2Se_3/ETL-free		0.52	−0.11	0.579	35.90	56.11	11.67
CuO/Sb_2Se_3/CdS		0.60	−0.03	0.537	34.93	67.71	12.71
CuSCN/Sb_2Se_3/CdS		0.60	−0.03	0.625	38.33	61.13	14.65
NiO/Sb_2Se_3/CdS		0.56	−0.07	0.627	37.82	68.67	16.31
CuI/Sb_2Se_3/CdS		0.50	−0.13	0.624	36.29	73.42	16.64
CuI/Sb_2Se_3/ETL-free		0.50	−0.13	0.691	36.64	75.28	19.08
(CuI-CuSCN)/Sb_2Se_3/CdS	Double	0.50	−0.03	0.629	38.12	78.66	18.87
(CuI-CuSCN)/Sb_2Se_3/ETL-free		0.50	−0.03	0.698	38.12	81.55	21.72

height (φ_p) value. Furthermore, Spiro-OMeTAD has low conductivity and a high negative VBO. Hence, the alignment of the band on both sides of the HTL is critical and should not be passed over. Table 7 provides the φ_p and VBO values for various HTL materials. CuI demonstrates the most exceptional performance, despite having the largest negative VBO among the HTL materials, due to its high conductivity and favorable band alignment with the front contact. The barrier height and hole mobility determine hole flow from the HTL towards the front electrode, with CuI showing the least kink effect overall.

To ensure the optimal design of the PV cell being studied, it is crucial to avoid the existence of the S-shape *J–V* behavior, resulting from the misalignment of the hole transport material with the FTO, as well as to pursue VBO engineering to achieve the highest possible PCE. To address these concerns, this study explores the utilization of a double HTL, consisting of CuI as an adjacent layer to the contact and CuSCN as an additional HTL, and investigates the double HTL cell performance with and without an ETL layer. The defect parameters at the CuI/CuSCN interface are the same as those for the HTL/absorber interface. The *J–V*

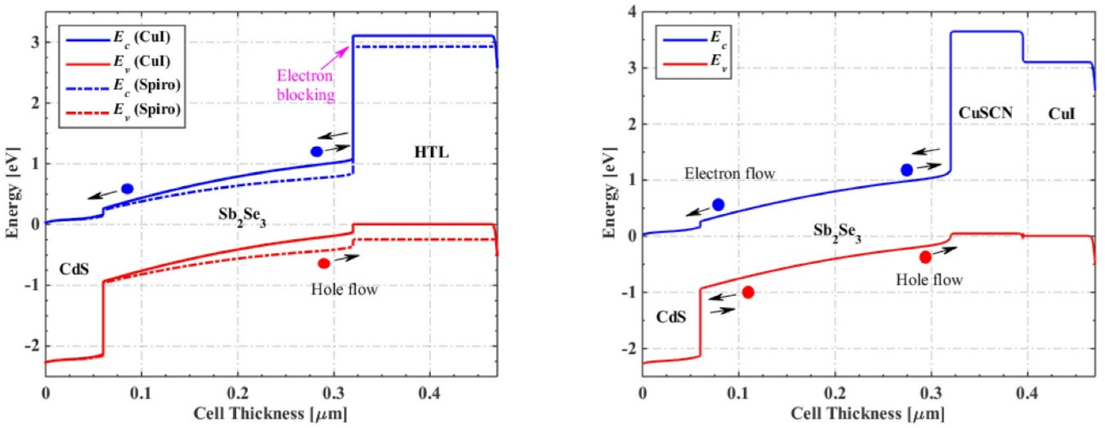

(a) (b)

Figure 8. Energy band profile at short circuit current condition under AM1.5G illumination for p-i-n Sb_2Se_3 cell with various HTL architectures (a) single HTL (Spiro & CuI), and (b) double HTL (CuI/CuSCN).

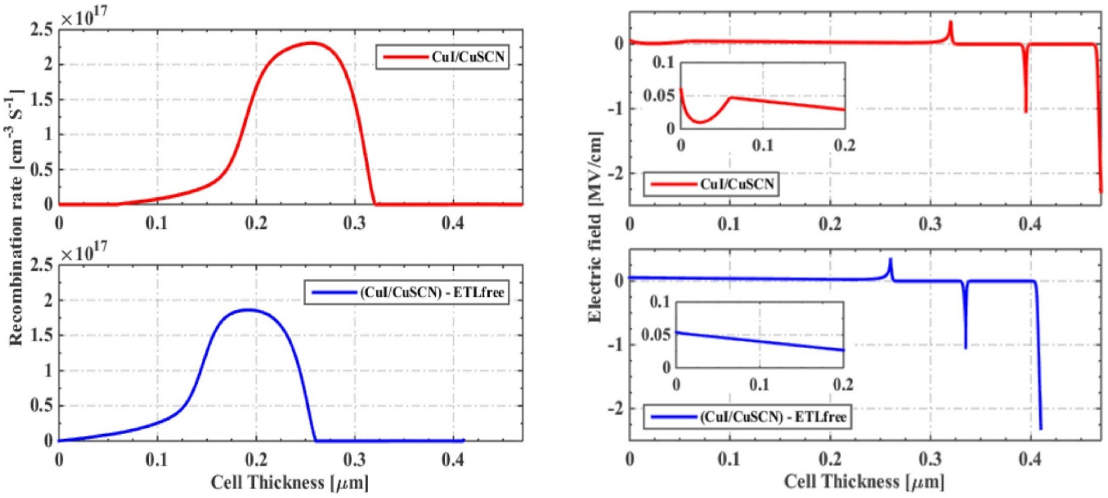

(a) (b)

Figure 9. (a) The recombination rate profiles, and (b) the electric field distribution plotted under illuminated short-circuit condition for p-i-n configuration with double HTL with and without ETL.

curves under illumination for these configurations are depicted in figure 7, and the results show significant improvement over the single HTL structure. Additionally, table 7 presents the PV parameters of all the investigated HTLs.

3.2.2. Physical interpretation of the results

To explain the observed trends when using a single HTL or a double HTL, the energy band profiles were created for three cases: single HTL using Spiro and CuI, and double HTL using CuI/CuSCN, as shown in figure 8. From figure 8(a), it can be inferred that although CuI has larger hole mobility and deeper electron barring properties than Spiro, its misalignment with the absorber creates a cliff-like band offset that deters the transport of holes. Although the cliff band case does not hinder the extraction of photoexcited holes from the photoactive film to the front electrode, it influences the activation energy related with charge carrier recombination, and thus interfacial recombination losses become the chief recombination mechanism within the PV cell [41, 42]. On the other hand, figure 8(b) demonstrates that using two HTLs results in a favorable band alignment with the absorber, creating an almost flat band that facilitates hole transport towards the FTO contact while also providing electron-blocking capabilities.

Moreover, to elucidate the observed improvement in performance parameters when utilizing a double HTL configuration with ETL-free, the recombination rate profile across the device distance at the illuminated short-circuit condition was created, as displayed in figure 9(a). The figure illustrates that using a double HTL configuration with ETL-free results in a decrease in the recombination rate in the Sb_2Se_3

Table 8. Comparison between the PV metrics for Sb_2Se_3 solar cell after various optimization steps.

	Transport layers					
Cell configuration	ETL	HTL	V_{oc} (V)	J_{sc} (mA cm^{-2})	*FF* (%)	*PCE* (%)
n-i-p	CdS	Spiro	0.466	33.64	67.06	10.51
	ZnSe		0.506	35.65	67.18	12.13
	ZnO-ZnSe		0.720	36.46	76.72	20.15
	CdS	HTL-free	0.467	33.15	65.97	10.23
	ZnSe		0.511	35.22	65.29	11.76
	ZnO-ZnSe		0.675	36.22	74.91	18.34
p-i-n	CdS	Spiro	0.511	35.46	51.47	9.33
		CuI	0.624	36.29	73.42	16.64
		CuI-CuSCN	0.629	38.12	78.66	18.87
	ETL-free	Spiro	0.579	35.90	56.11	11.67
		CuI	0.691	36.64	75.28	19.08
		CuI-CuSCN	0.698	38.12	81.55	21.72

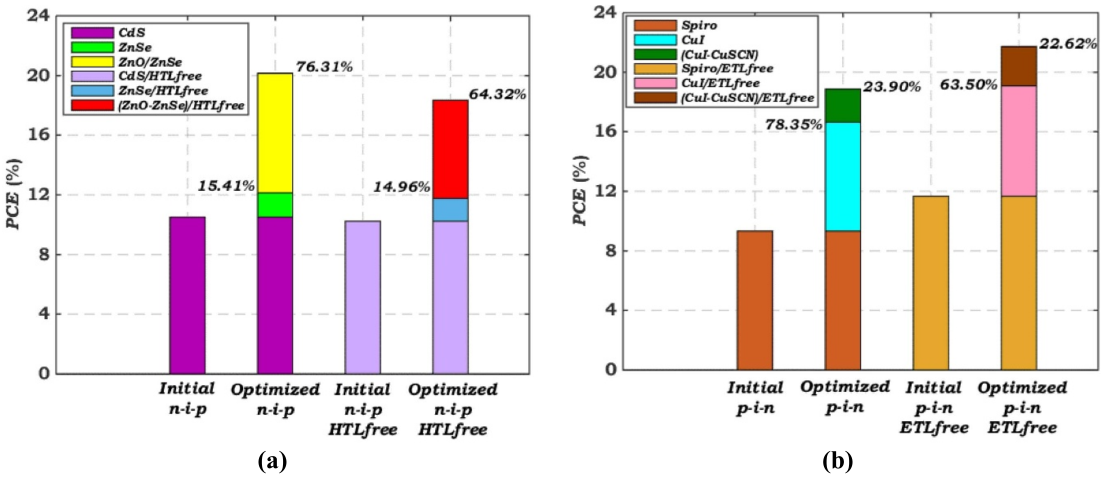

Figure 10. Efficiency advancements for various cases of Sb_2Se_3 cells with (a) n-i-p and (b) p-i-n configurations.

absorber, which enhances the cell performance. Additionally, the distribution of the electric field along the device structure, from ETL to HTL direction, at the illuminated short-circuit condition offers further evidence of the recombination behavior. This distribution is depicted in figure 9(b), where it can be observed that the electric field is greatest at the front contact/HTL interface for both configurations due to the HTL layer's high doping concentration. Also, a negative peak located at the CuI/CuSCN interface promotes the extraction of photogenerated holes from the absorber towards the front contact.

3.3. Final optimization

Table 8 presents the performance parameters of the Sb_2Se_3 solar cell after various optimization steps, and figure 10 shows the corresponding PCE values and the percentage improvement over the previous step. The results demonstrate that for the n-i-p structure, the dual ETL system of (ZnO-ZnSe) with Spiro-OMeTAD HTL achieved the highest PCE of 20.21%, with a relative enhancement of 92.29% in comparison with the initial calibrated Sb_2Se_3 cell. Conversely, for the p-i-n cell, the utilization of (CuI-CuSCN) as a dual HTL system without ETL resulted in the highest PCE of 21.72%, with a relative improvement of 86.12% in comparison with the initial inverted cell. This highlights the importance of utilizing dual transport layers and engineering the absorber-transport layer interface to reduce interface recombination and improve cell performance. Additionally, figure 11 illustrates the illuminated *J*–*V* characteristics and *EQE* spectra for the initial calibrated Sb_2Se_3 cell, the best n-i-p configuration cell (ZnO-ZnSe), and the best p-i-n configuration cell (CuI-CuSCN-ETL-free).

To gain physical insights into the observed outcomes, we performed simulations of the *J*–*V* dark characteristics to get the reverse saturation current (J_o) and the ideality factor (n). Figure 12 displays the *J*–*V* dark characteristics for the calibrated (initial), the best n-i-p configuration (ZnO-ZnSe double ETL), and the

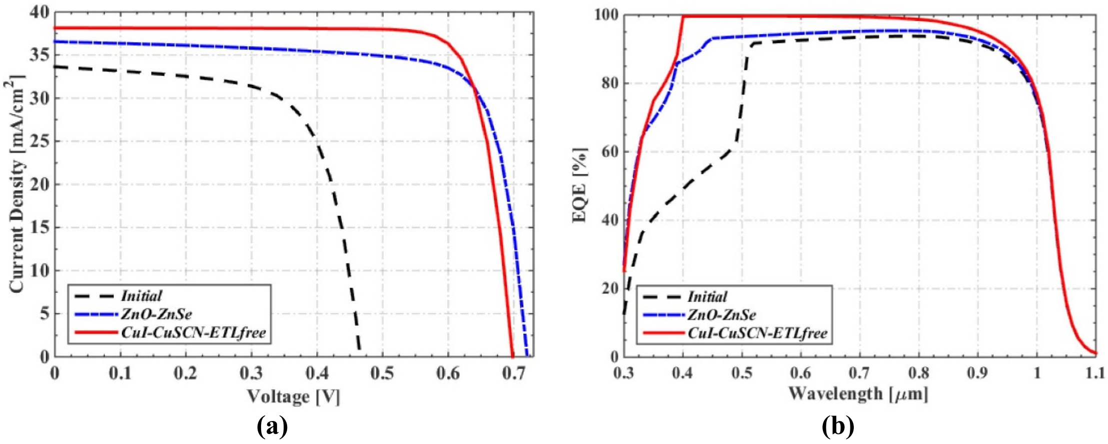

Figure 11. A comparison of (a) the *J–V* characteristics and (b) quantum efficiency concerning the initial calibrated Sb_2Se_3 cell, the best n-i-p configuration cell (ZnO-ZnSe), and the best p-i-n configuration cell (CuI-CuSCN-ETL-free).

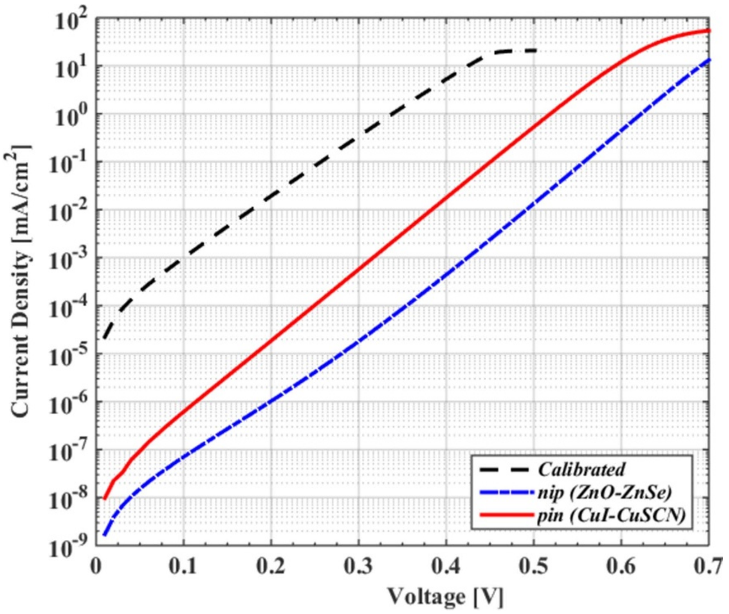

Figure 12. *J–V* dark characteristics of (a) calibrated Sb_2Se_3, (b) best n-i-p Sb_2Se_3 (ZnO-ZnSe), and (c) best p-i-n Sb_2Se_3 (CuI-CuSCN) cell (including ETL).

Table 9. Reverse saturation current and ideality factor of calibrated, best n-i-p (ZnO-ZnSe), and best p-i-n (CuI-CuSCN) (with ETL) Sb_2Se_3 cells.

	J_o (A cm^{-2})	n
Calibrated Sb_2Se_3	5.31×10^{-5}	1.32
n-i-p (ZnO-ZnSe) Sb_2Se_3	1.93×10^{-10}	1.08
p-i-n (CuI-CuSCN) Sb_2Se_3	1.98×10^{-8}	1.13

best p-i-n configuration (CuI-CuSCN double HTL) cells. To ensure a fair comparison, all three cells are considered with their respective carrier transport layers. Table 9 presents the extracted values of their reverse saturation current and ideality factor. It is evident that the n-i-p configuration cell exhibits the lowest reverse saturation current and ideality factor, while the initially calibrated cell shows the highest reverse saturation current and ideality factor.

The observed differences in the reverse saturation current and ideality factor among the three cells have significant physical consequences that directly influence their overall performance. The lower J_o and n values in the n-i-p configuration cell indicate reduced recombination and improved charge carrier collection efficiency at the contacts. This suggests that the n-i-p configuration cell has better electron-hole separation

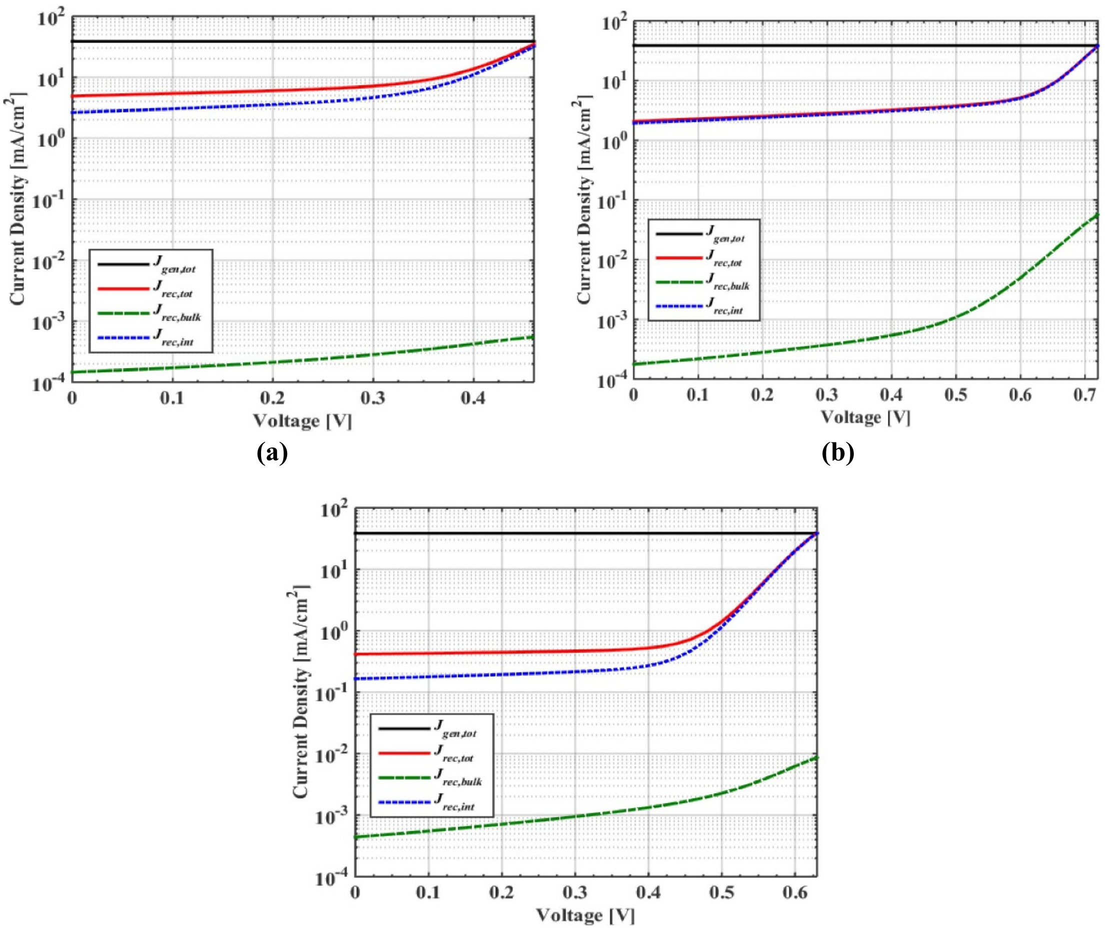

(a) (b) (c)

Figure 13. Current components of (a) calibrated Sb_2Se_3, (b) best n-i-p Sb_2Se_3 (ZnO-ZnSe), and (c) best p-i-n Sb_2Se_3 (CuI-CuSCN) cell (including ETL).

and less non-radiative recombination, leading to enhanced open circuit voltage and higher fill factor. On the other hand, the higher J_o and n values in the initially calibrated cell imply increased recombination and a less efficient charge carrier collection process. This results in reduced V_{oc} and FF, leading to lower overall PCE. Regarding the p-i-n structure, although the values of J_o and n are less than those for the initial cell, they are larger than the n-i-p cell values. As a result, the p-i-n structure exhibits reduced V_{oc} and PCE as quantitatively indicated in table 8.

Moreover, to distinguish between the different recombination mechanisms appearing in these solar cells, we provide a comparison between the interface-type and SRH-type recombination current densities. Figure 13 illustrates recombination current components at the interface ($J_{rec,int}$) and the bulk ($J_{rec,bulk}$) versus voltage up to V_{oc} for the three cases. The total generation ($J_{gen,tot}$) and recombination ($J_{rec,tot}$) current densities are also plotted. The figure indicates that $J_{rec,int}$ for the initial cell is higher than that for the optimized cases, whereas $J_{rec,bulk}$ is slightly higher for the two optimized cases when compared to the initial case.

Regarding interface recombination, it occurs at the contact interfaces between different layers of the solar cell, where charge carriers recombine before contributing to the overall photocurrent. Higher $J_{rec,int}$ indicates higher rate of recombination at these interfaces. The initial calibrated case shows the highest $J_{rec,int}$, suggesting that there is a higher loss of charge carriers at the interfaces. This leads to a reduced contribution of charge carriers to the overall current, resulting in a lower photocurrent. The p-i-n structure has the lowest $J_{rec,int}$, confirming the highest J_{sc} amongst the three cases (which is 38.12 mA cm^{-2}; see table 4). Optimized cell configurations (p-i-n and n-i-p) may have slightly higher bulk recombination compared to the initial cell, contributing to minor reduced V_{oc}, but other factors, such as improved charge extraction at the interfaces, lead to an overall enhancement in device performance. In addition, the higher $J_{rec,bulk}$ of p-i-n cell compared to n-i-p cell explains its lower V_{oc}.

The differences in the recombination current densities between the initial calibrated and optimized cases indicate that the optimizations have successfully reduced recombination losses, particularly at the interfaces, leading to improved charge carrier collection and higher photocurrent. These physical insights provide valuable information for understanding and enhancing the performance of the Sb_2Se_3 solar cells.

4. Conclusions

This study involved the design and simulation of p-i-n and n-i-p Sb_2Se_3-based solar cell structures using the SCAPS-1D device simulator. The simulation model, executed in the simulator, along with the physical and geometrical parameters are validated against a previously manufactured solar cell with the configuration FTO/CdS/Sb_2Se_3/Spiro-OMeTAD/Au that accomplished a PCE of 10.57%. We have examined the n-i-p configuration of the Sb_2Se_3 cell to determine the primary effects of the barrier height between the ETL and the front FTO contact and the CBO between the ETL and the absorber. We have also investigated the influence of different ETL materials. Our findings indicate that the inorganic material ZnSe is the most appropriate option, achieving a PCE of 12.13%. Further, a double ETL configuration was suggested, in which ZnO is positioned as the ETL adjacent to the FTO electrode to achieve an appropriate barrier height and facilitate electron transport towards the contact. Another ETL material in contact with the absorber is added to achieve a suitable CBO for electron flow. The system incorporating ZnO/ZnSe exhibits the best performance, with a PCE of 20.15%.

Furthermore, we investigated the p-i-n configuration by substituting the organic HTL material with different inorganic alternatives. The outcomes revealed that inorganic CuI material is the optimal choice, achieving a PCE of 19.08% with an ETL-free configuration. We also proposed a double HTL structure, in which CuI is an HTL adjacent to the FTO layer to achieve an appropriate barrier height and facilitate the transport of holes to the electrode. Further, the additional HTL adjacent to the CuI is put in contact with the Sb_2Se_3 layer to attain a proper VBO for hole transportation. The numerical results demonstrated that the CuI/CuSCN system, with an ETL-free configuration, exhibits the highest performance, with a PCE of 21.72%.

The results of the study suggest that the use of a p-i-n configuration with CuI/CuSCN as a double HTL and ETL-free holds great promise in creating a low-cost, highly efficient, and simple Sb_2Se_3 solar cell. As a next step, we aim to analyze the effect of altering the doping and thickness of cell layers, in order to further optimize the design. The current simulation work presents a possible means of increasing the efficiency of Sb_2Se_3-based solar cells, and as such, it could offer useful design recommendations for future experimental endeavors.

Data availability statement

The data that support the findings of this study are available upon reasonable request from the authors.

Acknowledgments

This research has been funded by Deputy for Research & Innovation, Ministry of Education through Initiative of Institutional Funding at University of Ha'il- Saudi Arabia through Project Number IFP—22188.

ORCID iDs

Marwa S Salem https://orcid.org/0000-0003-2107-8117
Mohamed Okil https://orcid.org/0000-0003-3816-3756
Ahmed Shaker https://orcid.org/0000-0001-6602-7343
Abdullah Albaker https://orcid.org/0000-0002-9902-9852

References

[1] Petrović-Ranđelović M, Kocić N and Stojanović-Ranđelović B 2020 The importance of renewable energy sources for sustainable development *Econ. Sustain. Dev.* **4** 15–24
[2] Green M A, Dunlop E D, Siefer G, Yoshita M, Kopidakis N, Bothe K and Hao X 2023 Solar cell efficiency tables (Version 61) *Prog. Photovolt., Res. Appl.* **31** 3–16
[3] Garnett E C and Yang P 2008 Silicon nanowire radial p-n junction solar cells *J. Am. Chem. Soc.* **130** 9224–5
[4] Putnam M C, Boettcher S W, Kelzenberg M D, Turner-Evans D B, Spurgeon J M, Warren E L, Briggs R M, Lewis N S and Atwater H A 2010 Si microwire-array solar cells *Energy Environ. Sci.* **3** 1037–41
[5] Salem M S, Alzahrani A J, Ramadan R A, Alanazi A, Shaker A, Abouelatta M, Gontrand C, Elbanna M and Zekry A 2020 Physically based analytical model of heavily doped silicon wafers based proposed solar cell microstructure *IEEE Access* **8** 138898–906

[6] Lu S, Chen C and Tang J 2020 Possible top cells for next-generation Si-based tandem solar cells *Front. Optoelectron.* **13** 246–55

[7] Lee T D and Ebong A U 2017 A review of thin film solar cell technologies and challenges *Renew. Sustain. Energy Rev.* **70** 1286–97

[8] Sahbel A, Hassan N, Abdelhameed M M and Zekry A 2013 Experimental performance characterization of photovoltaic modules using DAQ *Energy Proc.* **36** 323–32

[9] Zeng K, Xue D J and Tang J 2016 Antimony selenide thin-film solar cells *Semicond. Sci. Technol.* **31** 063001

[10] Chen C *et al* 2015 Optical properties of amorphous and polycrystalline Sb_2Se_3 thin films prepared by thermal evaporation *Appl. Phys. Lett.* **107** 043905

[11] Guo L, Zhang B, Ranjit S, Wall J, Saurav S, Hauser A J, Xing G, Li L, Qian X and Yan F 2019 Interface engineering via sputtered oxygenated CdS:O window layer for highly efficient Sb_2Se_3 thin-film solar cells with efficiency above 7% *Sol. RRL* **3** 1900225

[12] Sun D, Fang Y, Yan X, Shan W, Sun W and Meng Q 2021 Ultrafast broadband nonlinear optical response in Co-doped Sb_2Se_3 nanofilms at near-infrared *Front. Mater.* **8** 350

[13] Leng M, Luo M, Chen C, Qin S, Chen J, Zhong J and Tang J 2014 Selenization of Sb_2Se_3 absorber layer: an efficient step to improve device performance of CdS/Sb_2Se_3 solar cells *Appl. Phys. Lett.* **105** 083905

[14] Liu X, Chen C, Wang L, Zhong J, Luo M, Chen J, Xue D J, Li D, Zhou Y and Tang J 2015 Improving the performance of Sb_2Se_3 thin film solar cells over 4% by controlled addition of oxygen during film deposition *Prog. Photovolt., Res. Appl.* **23** 1828–36

[15] Mavlonov A *et al* 2020 A review of Sb_2Se_3 photovoltaic absorber materials and thin-film solar cells *Sol. Energy* **201** 227–46

[16] Zhao Y *et al* 2022 Regulating deposition kinetics via a novel additive-assisted chemical bath deposition technology enables fabrication of 10.57%-efficiency Sb_2Se_3 solar cells *Energy Environ. Sci.* **15** 5118–28

[17] Li Z *et al* 2019 9.2%-efficient core-shell structured antimony selenide nanorod array solar cells *Nat. Commun.* **10** 125

[18] Chen C *et al* 2017 6.5% certified efficiency Sb_2Se_3 solar cells using PbS colloidal quantum dot film as hole-transporting layer *ACS Energy Lett.* **2** 2125–32

[19] Liu D, Tang R, Ma Y, Jiang C, Lian W, Li G, Han W, Zhu C and Chen T 2021 Direct hydrothermal deposition of antimony triselenide films for efficient planar heterojunction solar cells *ACS Appl. Mater. Interfaces* **13** 18856–64

[20] Li G, Li Z, Liang X, Guo C, Shen K and Mai Y 2019 Improvement in Sb_2Se_3 solar cell efficiency through band alignment engineering at the buffer/absorber interface *ACS Appl. Mater. Interfaces* **11** 828–34

[21] Wen X *et al* 2018 Vapor transport deposition of antimony selenide thin film solar cells with 7.6% efficiency *Nat. Commun.* **9** 2179

[22] Chen G, Li X, Abbas M, Fu C, Su Z, Tang R, Chen S, Fan P and Liang G 2023 Tellurium doping inducing defect passivation for highly effective antimony selenide thin film solar cell *Nanomaterials* **13** 1240

[23] Jiménez T, Seuret-Jiménez D, Vigil-Galán O, Basurto-Pensado M A and Courel M 2018 Sb_2 $(S_{1-x}Se_x)_3$ solar cells: the impact of radiative and non-radiative loss mechanisms *J. Phys. D: Appl. Phys.* **51** 435501

[24] Lin L Y, Jiang L Q, Qiu Y and Fan B D 2018 Analysis of Sb_2Se_3/CdS based photovoltaic cell: a numerical simulation approach *J. Phys. Chem. Solids* **122** 19–24

[25] Cao Y, Zhu X, Chen H, Zhang X, Zhou J, Hu Z and Pang J 2019 Towards high efficiency inverted Sb_2Se_3 thin film solar cells *Sol. Energy Mater. Sol. Cells* **200** 109945

[26] Baig F, Khattak Y H, Beg S and Soucase B M 2019 Numerical analysis of a novel CNT/Cu_2O/Sb_2Se_3/In_2S_3/ITO antimony selenide solar cell *Optik* **197** 163107

[27] Gharibshahian I, Orouji A A and Sharbati S 2020 Towards high efficiency Cd-Free Sb_2Se_3 solar cells by the band alignment optimization *Sol. Energy Mater. Sol. Cells* **212** 110581

[28] Basak A and Singh U P 2021 Numerical modelling and analysis of earth abundant Sb_2S_3 and Sb_2Se_3 based solar cells using SCAPS-1D *Sol. Energy Mater. Sol. Cells* **230** 111184

[29] One Dimensional Solar Cell Simulation Program; SCAPS 3.3.10 Manual (available at: https://scaps.elis.ugent.be/SCAPSinstallatie.html)

[30] Salem M S, Shaker A, Zekry A, Abouelatta M, Alanazi A, Alshammari M T and Gontand C 2021 Analysis of hybrid hetero-homo junction lead-free perovskite solar cells by scaps simulator *Energies* **14** 5741

[31] Abdelaziz W, Zekry A, Shaker A and Abouelatta M 2020 Numerical study of organic graded bulk heterojunction solar cell using SCAPS simulation *Sol. Energy* **211** 375–82

[32] Salem M S, Shaker A, Abouelatta M, Alanazi A, Al-Dhlan K A and Almurayziq T S 2022 Numerical analysis of hole transport layer-free antimony selenide solar cells: possible routes for efficiency promotion *Opt. Mater.* **129** 112473

[33] Salem M S, Shaker A, Almurayziq T S and Alshammari M T 2022 Prospective efficiency boosting of full-inorganic single-junction $Sb_2(S, Se)_3$ solar cell *Sol. Energy Mater. Sol. Cells* **248** 112001

[34] Salem M S, Shaker A, Othman M S, Al-Bagawia A H, Fedawy M and Aleid G M 2022 Numerical analysis and design of high performance HTL-free antimony sulfide solar cells by SCAPS-1D *Opt. Mater.* **123** 111880

[35] Sood M, Gnanasambandan P, Adeleye D, Shukla S, Adjeroud N, Leturcq R and Siebentritt S 2022 Electrical barriers and their elimination by tuning (Zn,Mg)O buffer composition in $Cu(In,Ga)S_2$ solar cells: systematic approach to achieve over 14% power conversion efficiency *J. Phys. Energy* **4** 045005

[36] Abdelaziz W, Shaker A, Abouelatta M and Zekry A 2019 Possible efficiency boosting of non-fullerene acceptor solar cell using device simulation *Opt. Mater.* **91** 239–45

[37] Ayala-Mató F, Vigil-Galán O, Nicolás-Marín M M and Courel M 2021 Study of loss mechanisms on $Sb_2(S_{1-x}Se_x)_3$ solar cell with n–i–p structure: toward an efficiency promotion *Appl. Phys. Lett.* **118** 073903

[38] Amin A *et al* 2022 Enhanced efficiency and stability in Sb_2S_3 seed layer buffered Sb_2Se_3 solar cells *Adv. Mater. Interfaces* **9** 2200547

[39] Zhang H, Cheng J, Lin F, He H, Mao J, Wong K S, Jen A K Y and Choy W C H 2016 Pinhole-free and surface-nanostructured NiOx film by room-temperature solution process for high-performance flexible perovskite solar cells with good stability and reproducibility *ACS Nano* **10** 1503–11

[40] Leong W L, Ooi Z E, Sabba D, Yi C, Zakeeruddin S M, Graetzel M, Gordon J M, Katz E A and Mathews N 2016 Identifying fundamental limitations in halide perovskite solar cells *Adv. Mater.* **28** 2439–45

[41] Minemoto T and Murata M 2015 Theoretical analysis on effect of band offsets in perovskite solar cells *Sol. Energy Mater. Sol. Cells* **133** 8–14

[42] Okil M, Shaker A, Ahmed I S, Abdolkader T M and Salem M S 2023 Design and analysis of Sb_2S_3/Si thin film tandem solar cell *Sol. Energy Mater. Sol. Cells* **253** 112210

[43] He X, Wu L, Hao X, Zhang J, Li C, Wang W, Feng L and Du Z 2019 The band structures of $Zn_{1-x}Mg_xO(In)$ and the simulation of CdTe solar cells with a $Zn_{1-x}Mg_xO(In)$ window layer by SCAPS *Energies* **12** 291

[44] Deepthi Jayan K 2021 Enhancement of efficiency of $(FA)_2BiCuI_6$ based perovskite solar cells with inorganic transport layers *Opt. Mater.* **122** 111671

[45] Hossain M K, Rubel M H K, Toki G F I, Alam I, Rahman M F and Bencherif H 2022 Effect of various electron and hole transport layers on the performance of $CsPbI_3$-based perovskite solar cells: a numerical investigation in DFT, SCAPS-1D, and wxAMPS frameworks *ACS Omega* **7** 43210–30

[46] Bansal S and Aryal P 2016 Evaluation of new materials for electron and hole transport layers in perovskite-based solar cells through SCAPS-1D *Simulations 2016 IEEE 43rd Photovoltaic Specialists Conf. (PVSC)* (*Portland, OR, USA*, *05-10 June 2016*) (IEEE) pp 0747–50

[47] Kour N, Mehra R and Chandni C 2018 Efficient design of perovskite solar cell using mixed halide and copper oxide *Chin. Phys.* B **27** 018801